Prepared for submission to JINST

A Prototype Scintillating Fibre Beam Profile Monitor for Ion Therapy Beams

B.D. Leverington,[a,1] **M. Dziewiecki,**[a] **L. Renner,**[a] **R. Runze,**[a,2]

[a] *Physikalisches Institut, Universität D-69120 Heidelberg, Germany*

E-mail: leverington@physi.uni-heidelberg.de

Abstract: A prototype plastic scintillating fibre based beam profile monitor was tested at the Heidelberg Ion Therapy Centre / *Heidelberg Ionenstrahl Therapiezentrum* (HIT) in 2016 to determine its beam property reconstruction performance and the feasibility of further developing an expanded system. At HIT protons, helium, carbon, and oxygen ions are available for therapy and experiments. The beam can be scanned in two dimensions using fast deflection magnets. A tracking system is used to monitor beam position and to adjust scanner currents online. A new detector system with a finer granularity and without the drift time delay of the current MWPC system with a similar amount of material along the beamline would prove valuable in patient treatment. The sensitive detector components in the tested prototype detector are double-clad Kuraray SCSF-78MJ scintillating fibres with a diameter of 0.250 mm wound as a thin multi-layer ribbon. The scintillation light is detected at the end of the ribbon with Hamamatsu S11865-64 photodiode arrays with a pitch of 0.8 mm. Commercial or readily available readout electronics have been used to evaluate the system feasibility.

The results shown in this paper include the linearity with respect to beam intensity, the RMS of the beam intensity as measured by two planes, along with the RMS of the mean position, and the measured beam width RMS. The Signal-to-Noise ratio of the current system is also measured as an indicator of potential performance. Additionally, the non-linear light yield of the scintillating fibres as measured by the photodiode arrays is compared to two models which describe the light yield as a function of the ion stopping power and Lorentz β.

Keywords: Beam-line instrumentation; Instrumentation for heavy-ion accelerators; Instrumentation for particle-beam therapy; Instrumentation for hadron therapy; Instrumentation for heavy-ion therapy; Scintillators, scintillation and light emission processes; Scintillators and scintillating fibres and light guides;

[1] Corresponding author.

[2] Currently attending Northwestern University.

Contents

1 Introduction

The Heidelberg Ionenstrahl Therapiezentrum (HIT) is a radiation therapy facility located on the campus of the Heidelberg University Hospital. It is one of the first synchrotron facilities in Europe providing proton as well as heavy ion beams and is designed to support a raster scanning dose delivery method [1, 2]. An overview of the accelerator system at HIT is shown in Figure 1. Protons, helium, carbon and oxygen ions are available from three ion sources[1] and are accelerated to 7 MeV/u in the Injector Linac. The final accelerator stage takes place in a 65 m circumference synchrotron. As soon as the particles have reached the desired energy they are guided by the high energy beam transport line to one of the three patient treatment rooms or an experimental area. The ranges of energies and intensities available for each ion type are shown in Table 1.

The beam in the treatment and experimental areas can be steered over a $20\,\text{cm} \times 20\,\text{cm}$ area such that a pre-determined integrated fluence of particles can be deposited over a given area. Patient treatment plans are typically divided into voxels on the order of mm^3 with the penetration depth of the beam determined by the location of the Bragg peak. The beam position, width and intensity

[1] Each source can supply every ion type. Multiple sources allows for rapid switching without delays due to restarting the source.

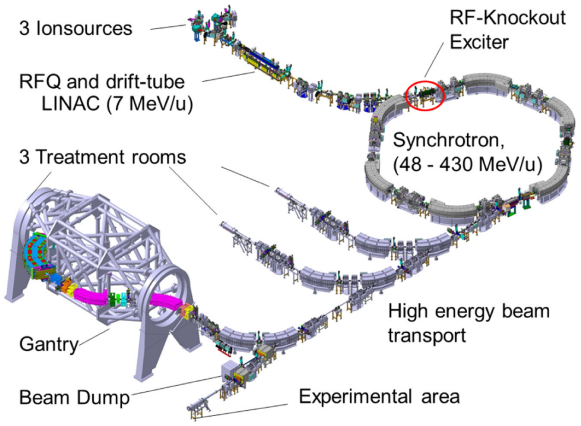

Figure 1: The HIT accelerator synchrotron complex with patient treatment rooms and an experimental area. Figure from [3].

	Protons	Helium	Carbon	Oxygen
Energy [MeV/u]	48–221	51–221	89–430	104–515
Intensity [s^{-1}]	$8{\cdot}10^7$–$3.2{\cdot}10^9$	$2{\cdot}10^7$–$8{\cdot}10^8$	$2{\cdot}10^6$–$8{\cdot}10^7$	$1{\cdot}10^6$–$4{\cdot}10^7$

Table 1: The energies and intensities available at the HIT Clinic. The energy range is divided into 255 possible settings, E1-E255. The intensities have 8-10 different settings available for use, I1-I10.

are monitored online by ionisation and multi-wire proportional chambers (IC and MWPC) placed 1-1.5 m upstream from the treatment iso-centre. A treatment plan is typically prepared such that the desired ionising radiation dose is deposited in the tumor with minimal dose being applied outside the treatment region. The stability of the intensity and position of the beam are monitored to ensure the correct dose is applied in each voxel, while also allowing for the intensity to be adjusted relative to the dose needed in each voxel [4].

In addition to patient treatment and clinical studies at the clinic, there is an ongoing effort to improve the accelerator facility as well. One such example is the rate of delivered dose. A decrease in the total treatment time due to higher beam rates would have multiple impacts. In addition to reduced patient treatment times and the corresponding increase in the number of patients per day that could be treated, the uncertainties in the position of the target dose volume would also decrease; Internal motions of the patient (such as respiration) can lead to uncertainties in the locations of the applied dose. There is interest at HIT for a new tracking detector system which will allow for these improvements at the end of the lifetime of the current system. The desired performance specifications for such a detector are summarised in Table 2 and are required over the beam settings specified in Table 1.

2 Detector

The proof-of-concept beam profile monitor (BPM) described in this paper is part of this research effort. In the current beam monitoring system at the HIT, a delay before switching to the next voxel

Table 2: The desired specifications for a beam profile monitor at HIT.

Requirement	Value
Beam Spot Size (FWHM)	1 – 33 mm
Beam Position Resolution	<0.2 mm
Beam Width Resolution	<0.4 mm
Readout Rate	4 – 8 kHz
Dead Time	<250 µs
Material in Active Area	<0.35 mm H_2O eq. / plane

of the treatment plan is introduced into the system due to the drift times of the ions produced in the gas of the MWPCs and ICs, which is approximately 150 µs or longer in length [4]. Additionally, the granularity of the MWPC is limited by the 2 mm wire spacing. A system based on scintillating fibres for beam position monitoring offers some benefits over the present system. Aside from the relative simplicity of constructing the sensitive detector plane, its robustness, and that gas and high voltage are not required, the fibres offer intrinsic benefits. The scintillation decay time is typically on the order of a few nanoseconds; the spatial granularity is proportional to the fibre diameter, which can be as low as 0.25 mm for plastic fibres; and the signal amplitude is proportional to the deposited energy in the fibre, though extensive research has shown this to be non-linear with increasing stopping power, dE/dx, for plastic scintillator, and will be examined in detail below. Photodiode arrays with a channel pitch of 0.8 mm are used to measure the light output with integration times of the photodiode array down to 100 µs. Covering the desired acceptance of 20 cm × 20 cm is also straight forward with scintillating fibres thanks to the production methods developed for the fibre tracker for the upgraded LHCb experiment at CERN [5] . The measurements ongoing at HIT aim to determine the feasibility of the scintillating fibre-based detector over the broad range of intensities and energies of the beam. The measured performance of the already available components presented in this paper will be used to develop subsequent detector prototypes.

2.1 Scintillating fibres

The scintillating fibre ribbon used in this research were produced originally by the LCHb Scintillating Fibre Tracker collaboration. The fibres are Kuraray SCSF-78MJ 0.25 mm diameter double-clad fibres wound into a multi-layer ribbon on a custom machine [6]. The emission spectra of these fibres peak at 450 nm[2]. The fibres have been bonded with a titanium dioxide(20% w/w) loaded two-component epoxy[3]. The overall thickness of the five layer mat is approximately 1.2 mm, larger than the 0.8 mm acceptance of the photodiode channel. This is also significantly more material than specified in Table 2. If the technology proves to be feasible, two layer mats with a mean thickness of 0.45 mm will be produced where multiple scattering of the ions will be comparable to the MWPC chambers. However, the thicker mats used in this measurement will still provide the information

[2]While not directly confirmed by the manufacturer, the polystyrene core is known to be doped with p-terphynyl (1% w/w) as the primary dopant and TPB (tetraphynyl-butadiene) (0.1% w/w) as the wavelength shifter. The cladding is PMMA based.

[3]Epotek 301-2

needed to evaluate the dynamic range and other performance characteristics.

The ribbons tested were 20 cm long[4] and the width covered by the photosensor was 51.2 mm. The standard horizontal fibre pitch is larger than the fibre diameter (0.275 mm) to accommodate small diameter variations. The proof-of-concept detectors studied here were produced by cutting a standard 2.5 m LHCb fibre ribbon that was available to us at the time in order to produce the shorter detector planes. Each ribbon is bonded between two PVC frames and the ends are milled with a single-point diamond blade to produce a high quality optical finish. The photodetectors are mounted at the end of the PVC frame for optical readout of the fibre mat. On either face of the fibre ribbon a 25 µm black polyimide foil is glued to improve the structural stability of the fibre mat and provides some shielding against stray light. Mirrors have not been used here but are considered for use in the future. The detector plane schematic is shown in Figure 2.

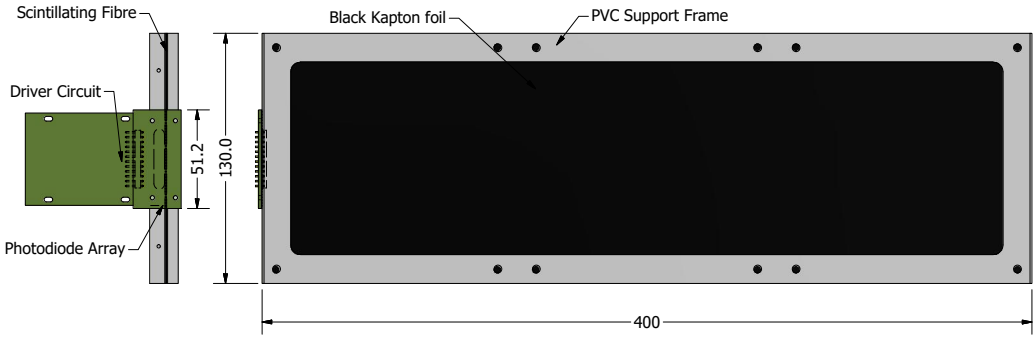

Figure 2: A drawing of a single 13 cm wide mat with a single photodiode array attached. The fibres are aligned in the horizontal direction.

2.2 Photodiode arrays

The beam width at the current tracking detector (MWPC) locations can be as small as 1 mm FWHM such that the granularity of the tracking planes should be the same or smaller. The Hamamatsu S11865-64 photodiode arrays used here have 64 channels with a pitch of 0.8 mm, covering 51.2 mm per array[5]. The pixel sizes are 0.7 mm × 0.8 mm (WxH). The limited pixel height means that not all of the 1.2 mm thickness of the fibre mat is readout for the 5-layer mat. The photosensitivity of the array peaks at 700 nm and matches well with the wavelength emission of the scintillating fibre.

The analog signal processing is performed by an onboard CMOS chip. The channels are integrated simultaneously and readout sequentially. The maximum readout rate is 12.5 kHz per 64 channel array. The C9118 driver circuit from Hamamatsu has been used to interface the array to the data acquisition system. The amplitude of the video output, which corresponds to the integrated charge of each channel, has been measured using the Heidelberg LogicBox system with a single channel SU735-2 12-bit ADC module [7]. The integration windows can be adjusted by the timing

[4]The width of the mat is currently limited to 13 cm by the production wheel used to wind the mat, and the length can be as long as 2.4 m.

[5]A 128-ch version of the photodiode array is available, but the intent will be to readout multiple arrays in the future in parallel. For a similar clock speed, the readout rate per array is two times faster for 64-ch arrays.

of control signals, and values from 25 µs up to 2500 µs are possible. Additionally, a gain can be selected from two values, low or high, which differ by a factor of two. The data transfer from the LogicBox to a PC uses the USB 2.0 protocol, which creates a readout limitation of 1-3 kHz. The future improvements to this system will attempt to achieve a readout rate for the complete system greater than 10 kHz with a dead time of less than 5% (5 µ sec) for multiple arrays. This is a significant improvement over the gas detectors with dead times (drift times) of more than 100 µ sec.

It should be noted that a similar prototype detector to the one constructed here with the same photodiodes[6] and readout electronics has been developed previously by Rojatti et al. [8] for the CNAO proton and carbon ion beamline in Italy but with 0.5 mm square fibres, covering a much smaller area (6 cm × 6 cm), a slower readout rate of 300 Hz, and a much longer integration time of 2.5 m sec. Comparable performance results from the CNAO detector have not been published.

3 Results

During the development of the detector, it was not clear from the outset how the detector would respond over the range of energies and intensities available at HIT for the different ion types. The results presented here are measurements over intensity or energy, to observe the response of the detector system test for linearity and dynamic range of the photodiodes coupled to the scintillating fibres and with the LogicBox readout. A lab measurement was first made with a UV source with subsequent measurements performed in the ion beamline.

3.1 Linearity with a UV light source

A UV(380 nm) LED was used to excite the wavelength shifting component of the scintillator while a calibrated photodiode[7] was used to monitor the intensity of the LED. In Figure 3, the relative measured intensity in ADC counts in the central channel is plotted versus the current measured in the calibrated photodiode. The response of the scintillating fibres and the photodiode arrays together is quite linear over the range of interest, but begins to deviate from linearity on the percent level towards the saturation limit of the ADC. This is likely due to a small internal resistance over which the potential drops with increasing photodiode current. The maximum signal observed from the ion beam is indicated for comparison, showing that the system is a safe distance from saturation when the integration window is the nominal 100 µs in length while having a moderate dynamic range. The electrical noise observed in the system during this test is quite small, with a pedestal width[8] of 12 ADC channels.

3.2 Beamline Measurement Setup

The experimental room at HIT provides a horizontal beam with a laser alignment system indicating the iso-center, where the beam properties are regularly checked during quality assurance measurements, and targets are typically placed. The BPM detector planes have also been placed at this location.

[6] The 128-ch version of the photodiode was used here.
[7] Newport 818-UV
[8] one sigma

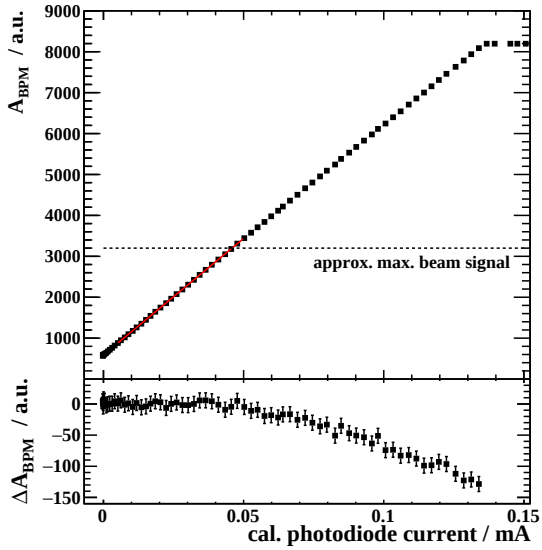

Figure 3: The linearity of the scintillating fibres coupled to the silicon arrays is shown in the top plot for a 370 nm UV light-source. The light intensity is measured with a calibrated photodiode for a single channel. The maximum signal amplitude seen in beam data is overlaid for comparison. A linear approximation is based on the lower third of the data (solid line). The difference of the data with respect to the approximated line is shown in the bottom plot.

In some measurements two detector planes have been used. The second plane was placed a short distance behind the first which was at the iso-center. The additional readout was connected in serial to the first and resulted in a reduction in overall readout rate due to the limited bandwidth of the available electronics.

The collected data has the form of beam profiles collected at a given frequency and integration time. Examples for proton, helium, carbon and oxygen beams are shown in Figure 4 for the highest possible energy setting as well as the lowest setting where the intensity is stable. An intensity setting of I8 was used for all the examples, though the average fluence depends on the ion species.

3.3 Response to Ion Beam Intensity

The intensity of the beam can be controlled by the user at the HIT clinic with nine or ten available settings, I1-I9/10. I10 is not always available for every ion type. For protons and carbon, this corresponds to $8 \cdot 10^7 - 3.2 \cdot 10^9 s^{-1}$ (I1-I0) and $2 \cdot 10^6 - 5 \cdot 10^7 s^{-1}$(I1-I9), respectively. The relative signal amplitude for the selected range of proton and carbon ion fluences is shown in Figures 5a and 5b. An integration time of 312 µs has been used with a low gain setting. A straight line is fit to the data to demonstrate the excellent linearity of the detector. This result is not entirely unexpected as the maximum density of particles is of the order of $1\,ns^{-1}cm^{-2}$ with a scintillator decay time of 2.36 ns [9]. The molecular excitation of the scintillator is highly localised and the probability of the scintillator being in an excited state is nearly zero for the next incident particle.

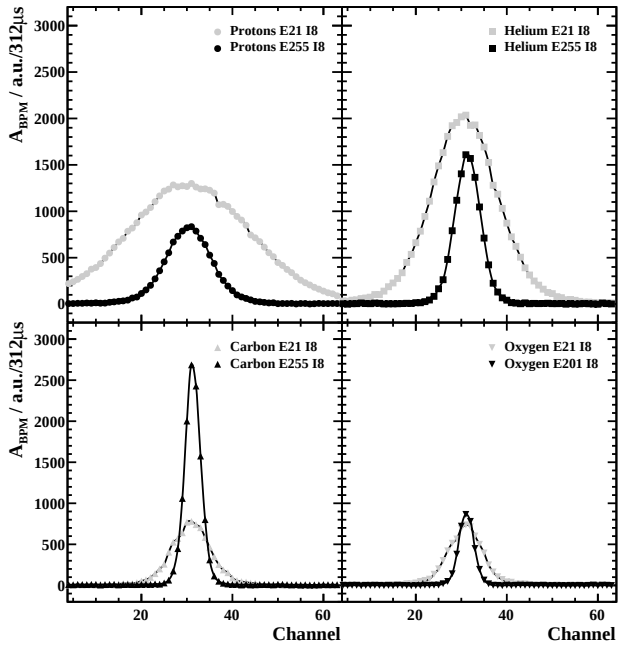

Figure 4: The observed signal amplitudes in a single 312 µs integration window with proton, helium, carbon and oxygen beams for two energy settings (highest and lowest with stable intensity) at a single intensity setting, I8.

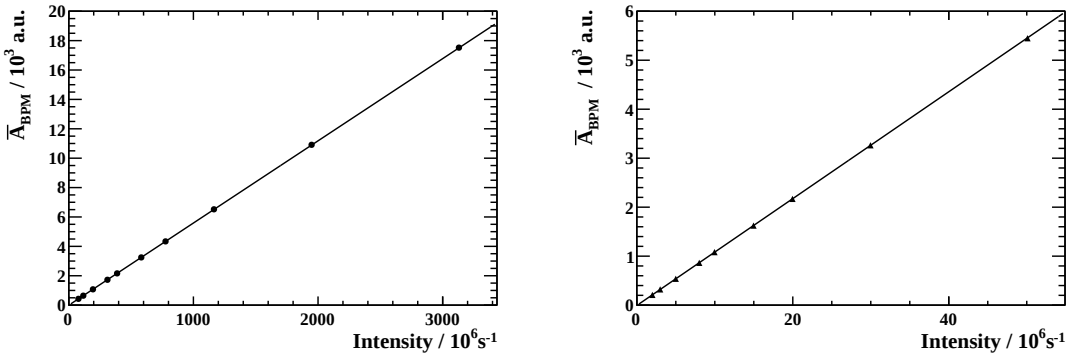

(a) Protons (b) Carbon

Figure 5: The relative signal amplitude for the available proton (221 MeV/u) and carbon (430 MeV/u) beam intensities, I1-I10.

3.4 Response to Ion Beam Energy and Species

It is well known that the light yield of plastic scintillator is dependent upon the dE/dx of the particle depositing energy in the base scintillator. However, the literature available for this particular scintillating fibre does not extend to heavier ions. The measurements here will show the relative signal response of the 0.250 mm diameter Kuraray SCSF-78MJ scintillating fibres to the available ions species (protons, helium, carbon, and oxygen) over their available range of energies. The stopping powers have been calculated using the PSTAR and ASTAR databases provided by NIST for protons and helium in polystyrene[10, 11]. Stopping powers for carbon and oxygen are derived from the MSTAR database[12].

The measured light yield response of the scintillating fibre is plotted as a function of the stopping power in polystyrene in Figure 6a on a linear scale. The same is visible in Figure 6b on a log-log scale to make the proton and helium data more visible.

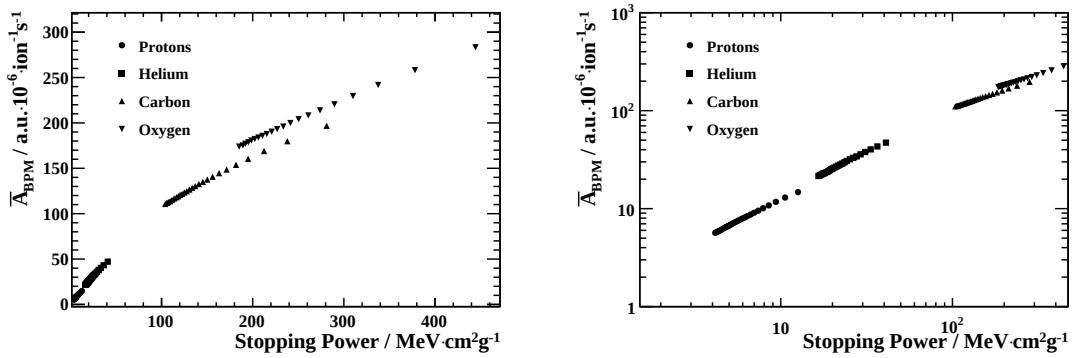

(a) Linear Scale

(b) Log-Log Scale

Figure 6: The signal amplitude per particle per second for the four different ion types plotted as a function of their stopping power in polystyrene.

Several models exist that describe the non-linear features observed in ion-induced scintillation. Birks first proposed that the specific scintillation signal amplitude per ion, A_{ion}, as a function of the stopping power can be described by [13]:

$$\frac{A_{ion}}{dx} = C_B \frac{dE/dx}{1 + k_B \cdot (dE/dx)}, \tag{3.1}$$

where k_B is generally referred to as the quenching parameter, and is known to be ion charge dependent. C_B is a signal gain parameter. A combined least-squares fit to the data in Figure 6a with Eq.3.1 using the Minuit2 package of ROOT6[14] results in the values listed in Table 3. The values for k_B are consistent with others found in the other literature cited here, between 2 and 20 mg $\cdot$ MeV^{-1}cm^{-2} and increases for decreasing Z.

Additional models developed since Birks' first measurements describe the energy deposition and saturation as the result of physical processes, typically described by a core region, in which the scintillator becomes saturated, and a halo, in which higher energy delta electrons have escaped the saturated core and the light yield is again linear to the deposited energy. One such model,

introduced by Tarlé [15] and Ahlen [16], following the work of Voltz et al. [17], describes the scintillation yield as:

$$\frac{A_{ion}}{dx} = C_{BVT}\frac{dE}{dx}\cdot\left(\frac{1-F_h}{1+B_S(1-F_h)dE/dx}+F_h\right), \tag{3.2}$$

where C_{BVT} is a gain parameter and B_S is the linear saturation coefficient. This will be referred to later as the BVT model. The fraction of scintillation light produced in the halo, F_h, is a function of the Lorentz parameters β and γ, as shown in Eq. 3.3, with an adjusted ionisation potential, $I_{ps} = 68.7$ eV, for polystyrene, and a free parameter, T_0, which can be interpreted as something like the minimum energy of the delta rays needed to escape the saturated core.

$$F_h = \frac{1}{2}\frac{ln(2mc^2\beta^2\gamma^2/T_0)-\beta^2}{ln(2mc^2\beta^2\gamma^2/I_{ps})-\beta^2} \tag{3.3}$$

	Birks Model	BVT Model
Protons	$k_B = 17.8 \pm 0.5\ mg\cdot MeV^{-1}cm^{-2}$	$T_0 = 1.3 \pm 0.4\ GeV$
Helium	$k_B = 6.8 \pm 0.2\ mg\cdot MeV^{-1}cm^{-2}$	$T_0 = 280 \pm 56\ keV$
Carbon	$k_B = 3.89 \pm 0.05\ mg\cdot MeV^{-1}cm^{-2}$	$T_0 = 33 \pm 4\ keV$
Oxygen	$k_B = 3.11 \pm 0.02\ mg\cdot MeV^{-1}cm^{-2}$	$T_0 = 15 \pm 2\ keV$
		$B_S = 5.4 \pm 0.2\ mg\cdot\ MeV^{-1}cm^{-2}$
	$\chi^2/ndf = 191/94$	$\chi^2/ndf = 142/93$

Table 3: The results of fitting Eq. 3.1 and Eq. 3.2 to the data in Figure 7. Each function is simultaneously fit to the four ion data sets. Similar gain constants of $C_B = (1.461 \pm 0.005)$ and $C_{BVT} = (1.425 \pm 0.004)\cdot 10^{-6}$a.u./(MeV $\cdot$ ion $\cdot$ s^{-1}) are found in the fits.

Given that both F_h and the stopping power, dE/dx, are dependent only on the ion charge and Lorentz β (Bethe-Bloch), it makes more sense to examine $dA/dE = dA/dx\cdot dx/dE$ as a function of β, as shown in Figure 7. A combined fit of all four data sets to Eq. 3.2 produces a single value of $B_S = 5.4 \pm 0.2$ mg $\cdot$ MeV^{-1}cm^{-2}. This is consistent with the result from Broggio et al.[18] where fixed energy Helium (150 MeV/u), Carbon (290 MeV/u) and Neon (400 MeV/u) ions were incident on a vinyltoluene plastic scintillator, and PMMA blocks were used to reduce the ion energy before the scintillator. The combined fit to our data was also constrained to a single value of C_{BVT} and produces a reasonable $\chi^2/ndf = 142/93$, which is slightly smaller than that of the Birks Model fit.

Requiring a single value of T_0 for all data sets did not produce a good result when fit to our data, especially the proton data. As such, T_0 was left as a free parameter for each data set. It can be seen that the value for oxygen agrees well with the other large Z measurements in [16] and [18]. However, the value for protons appears unphysical, as the kinematic limit for delta ray production by heavy charged particles is $T_{max} = 2m_ec^2\beta^2\gamma^2 < 600$ keV for protons with $\beta < 0.6$. Despite this, the increasing values for T_0 for decreasing Z is consistent with the core-halo model, such that increasing values of T_0 indicate that an increasing amount of the scintillation light is produced in the saturated core region and increasingly higher energy delta electrons are required to reach an unsaturated halo region. In the case of protons, this would mean that the entire region is saturated

as no delta rays are energetic enough to escape to an unsaturated halo and the saturation per unit energy deposited is much larger than for higher Z ions, as can be observed in the matching Birks coefficient, k_B.

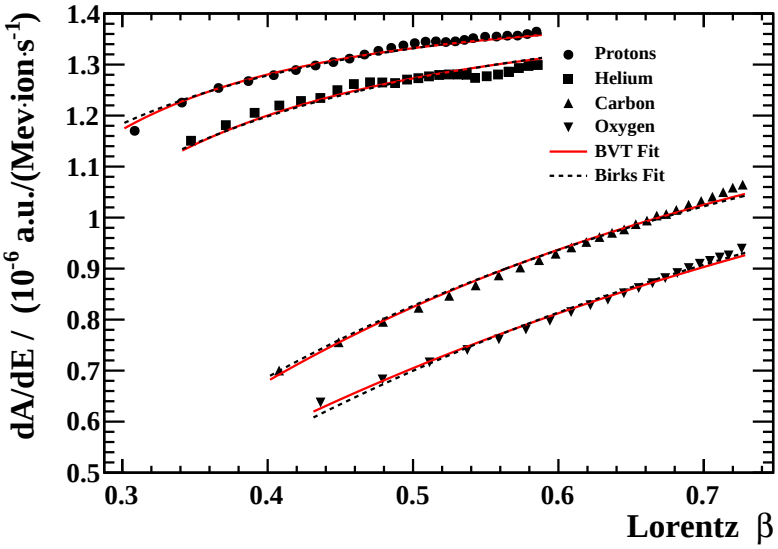

Figure 7: The scintillation yield per 10^6 ions per second per unit energy deposited as a function of Lorentz β for protons, helium, carbon, and oxygen ions measured at HIT.

3.5 Detector Performance

In the following measurements, two detector planes were used with a readout rate of 1 kHz and a single integration time close to the desired operational value of 100 µs with a high gain setting. Data was only collected for proton and carbon beams in this measurement as they are the two ion species used for patient treatment so far.

3.5.1 Signal-to-noise Ratio

The signal-to-noise ratio (SNR) of the detector is an important parameter in being able to extract correctly the beam position, intensity and width. Here we have defined the SNR as half the mean peak amplitude for each intensity setting divided by the standard deviation of the baseline noise, σ_{noise}. The position downstream of the currently installed tracking detectors will result in a wider beam (due to multiple scattering) relative to the few mm beam width at the MWPC locations. This naturally decreases the SNR such that an improved value would be expected in real use. In Figure 8, the lowest three intensity settings have an SNR less than five and the performance will likely be adversely affected by the electronics noise for the beam settings measured. The error bars in the figure are the RMS of the peak amplitude distribution to σ_{noise} ratio, such that, even for higher intensities, some integration windows will have an SNR less than five. Improved dedicated electronics and additional shielding will likely improve the SNR in a further iteration of this detector system. Moving the detector further upstream would also result in more light per channel along with the use of a mirror. An increased integration period could also improve the SNR and would be feasible at

low intensities but would limit the readout rate of the beam position to a value similar to the MWPCs.

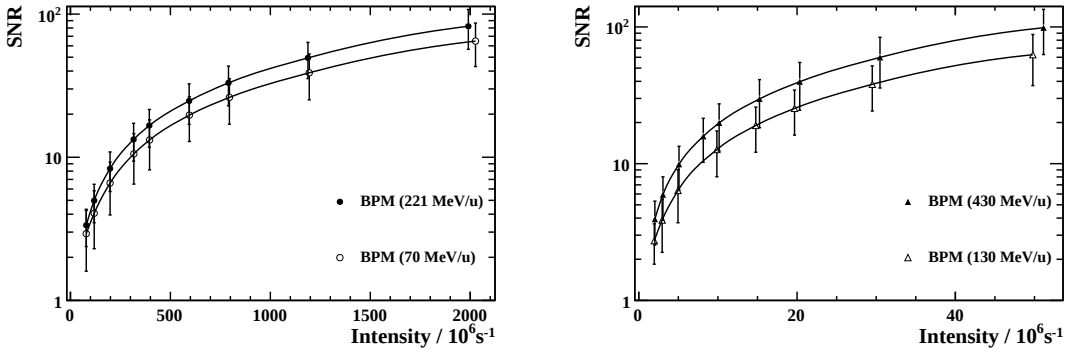

(a) Protons (b) Carbon

Figure 8: The signal-to-noise ratio for the available proton and carbon beam intensities and two energy settings, E21 and E255. An integration period of 100 µs was used with a high gain setting. The error bars are the RMS of the peak amplitude distribution to σ_{noise} ratio, which is dominated by the beam structure over time. The wider beam at the iso-center for the lower energy ions produces a worse SNR for the same intensity despite the slightly larger dE/dx.

3.5.2 Beam Position Resolution

The mean position in each detector plane is determined from a Gaussian fit to the detector data and compared to the second detector plane. The per plane beam position resolution is given in Figure 9 for proton and carbon ion beams where the detector has been placed at the treatment iso-center. The clinic requires that any new tracking system be able to resolve a beam with a FWHM of about 1 mm with a position resolution better than 0.2 mm. The distance further downstream from the nominal tracking station positions means the beam has broadened significantly and achieving this with a low energy proton beam is not likely. The broad beam and the low SNR results in a position resolution of 0.45 mm for the lowest intensity and low energy proton beam, improving to less than 30 µm for the highest intensity. The highest energy has a top resolution of 12 µm. The MWPC tracking chambers currently used by the clinic are placed 1.0−1.5 metres further upstream. However, the beam profile for carbon ions is less affected by multiple scattering in the detector systems, and, as such, is a better representation of the performance of the BPM as a tracking detector. A position resolution of 0.28 mm is achieved for the lowest intensity and low energy carbon beam and the highest intensity and energy achieves a position resolution of 10 µm. Future measurements will attempt to move as far as possible upstream.

3.5.3 Beam Width Resolution

Correctly reconstructing the beam width is as important for patient treatment as the beam position, as the correct distribution of dose amongst voxels needs to be determined. The clinic has asked that the width resolution be determined better than 0.4 mm for the tracking stations. The standard deviation of the difference in the measured beam width between the two detector planes, $\sigma(F_1 - F_2)/\sqrt{2}$

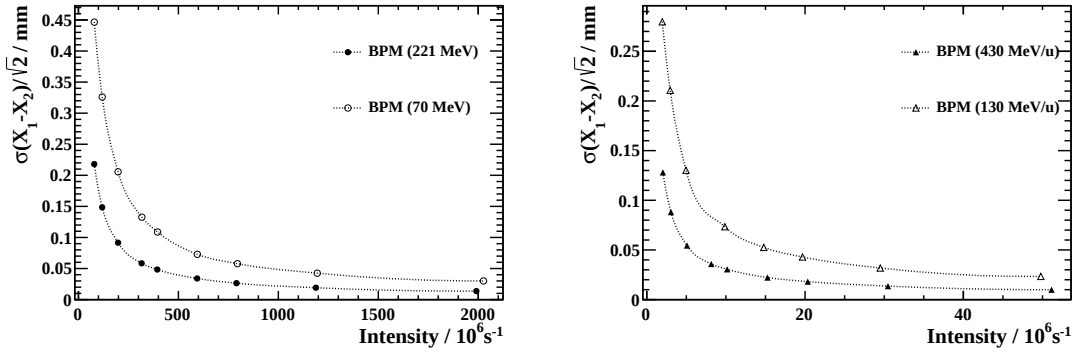

(a) Protons (b) Carbon

Figure 9: The beam position resolution for the available proton and carbon beam intensities and two energy settings, E21 and E255. An integration period of 100 µs was used with a high gain setting.

is shown in Figure 10. As can be seen in the figure, $\sigma(F_1 - F_2)/\sqrt{2} = 3.5$ mm for a single detector plane for the lowest intensity 70 MeV protons and the highest intensity 221 MeV proton beam width has a resolution of 0.044 mm. In general, the low intensity proton beam width is not reconstructed as well as desired. This is again dominated by the poor SNR and the beam being broader than the photodetector. The narrower carbon beams are better reconstructed with a resolution of $\sigma(F_1 - F_2)/\sqrt{2} = 0.98$ mm for low intensity 130 MeV/u ions and, for high intensity 430 MeV/u ions, the width resolution is as low as $\sigma(F_1 - F_2)/\sqrt{2} = 0.03$ mm. Much like the beam position resolution, these values will likely improve as the tracking planes are moved further upstream, the absolute width of the beam narrows, and the SNR improves.

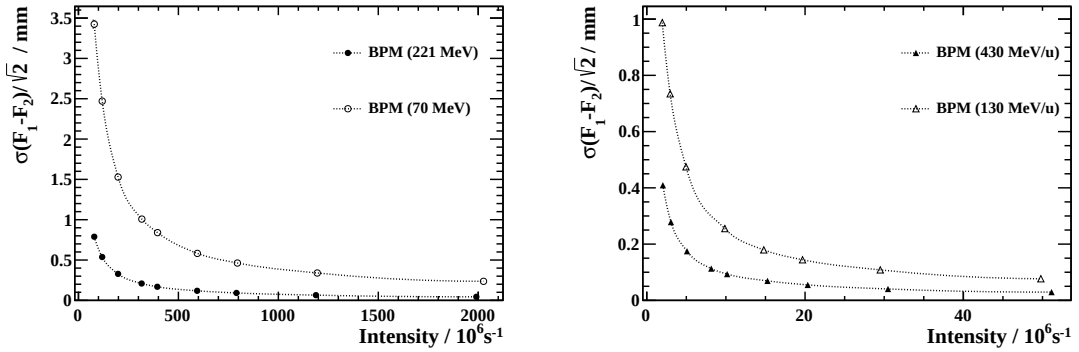

(a) Protons (b) Carbon

Figure 10: The absolute beam width/focus (FWHM) resolution for the available proton and carbon beam intensities and two energy settings, E21 and E255. An integration period of 100 µs was used with a high gain setting.

3.5.4 Signal Amplitude Resolution

The purpose of the BPM is to primarily monitor the position and width of the beam. However, given the predictable response of the scintillator to each ion type and intensity, it may be possible to use the detector as a secondary dose monitor complimentary to the ionisation chambers already installed. A measure of the dose measurement performance is the signal resolution. The signal resolution in each 100 µs integration window, or the sigma of the difference in signal amplitude[9] divided by the mean signal amplitude plotted as a function of the beam intensity, is shown in Figure 11 for protons and carbon ions. A small correction is applied to the gain of the second detector plane amplitude to provide the same mean signal amplitude. The additional division by $\sqrt{2}$ provides the single detector plane resolution, as the two planes are identical in design and construction with some residual differences remaining in the fibre light yield, transmission, and the photodiode array gain. For comparison, the same calculation for the ionisation chamber (IC) data provided by the EtherCAT system at HIT is plotted. Here, the ionisation current from two ionisation chambers is provided in 50 µs intervals via EtherCat and a timestamp is injected into the asynchronous readout systems for offline time alignment. The IC data is then averaged over the equivalent photodiode integration window for this analysis. For operational and safety purposes at the Clinic, the IC current is monitored via a different system with faster time scale on the order of 1 µs[10].

As can been seen in Figures 11a and 11b, the performance is strongly dependent on the intensity of the beam. As expected from the SNR, the lower intensities suffer in performance but for the majority of the intensity settings, the signal resolution is comparable to or better than that observed in the IC data. However, the IC data is quite flat over the range of intensities. Ideally, the total dose for each treatment voxel should be known to the order of 0.5% and with the treatment time per voxel on the order of milliseconds, the resolution per 100 µs integration should be much better than 10% and closer to 2–3%. For high intensities, the current state of the BPM is sufficient. However, scientists from the clinic have communicated that the intensity used during patient treatment is typically at the lower end of the scale. Improvements in the SNR from increased integration times, as well as reduced electronics noise, will directly improve the signal resolution in future developments.

4 Challenges

Two primary concerns exist regarding a detector of this construction. The first is the amount of material in the beam line before the patient. Ideally, multiple scattering and secondary production should be minimised.[11] To this end, two layer fibre mats will be custom produced for new detector prototypes. The reduced scintillator thickness will better match the photodiode height without the loss of light. The material thickness then reduces to approximately 0.45 mm per detector plane. The current gas-based chambers represents approximately 0.35 mm of water-equivalent material on average.

The second challenge is the radiation damage induced in the plastic scintillating fibres. While the total dose expected in one year over the surface of the fibre area is relatively low from patient treatment, the total fluence through the central point of the detector plane from regular accelerator

[9] After correction for a small difference in gain.

[10] It is potentially feasible to implement a fast current readout on the photodiode arrays as well.

[11] A five layer fibre mat is contains approximately 0.35% of a radiation length of material in the beam line.

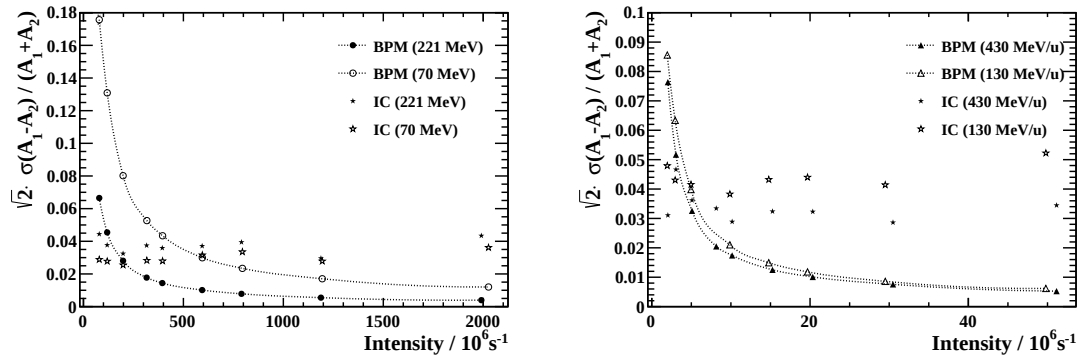

(a) Protons

(b) Carbon

Figure 11: The signal resolution for the available proton and carbon beam intensities and two energy settings, E21 and E255. An integration period of 100 µs was used with a high gain setting.

activities is very high, >1 MGy, producing a few mm wide darkened spot. It is well known that the transmission of plastic scintillator is reduced with a strong wavelength dependence and has been measured up to 35 kGy for this particular fibre [19]. Primarily the blue component is blocked leading to the yellowing of the fibres. As the decay times of the all fibres are very fast compared to the integration window we intend to use, a slower but more radiation hard fibre like 3HF will be investigated. The 3HF fibres emit light with a peak wavelength of 530 nm which also matches better with the spectral sensitivity of the photodiode which peaks at 700 nm. Additionally, a filter may reduce the sensitivity to the change in certain wavelengths due to radiation damage. A mirror would also increase the total light yield collected at the photodiode improving the SNR.

5 Conclusion

We have measured the scintillation response of Kuraray SCSF-78MJ scintillating fibres to proton, helium, carbon and oxygen ion beams over the range of energies and intensities used at the Heidelberg Ion Therapy Clinic. The linearity and dynamic range of the fibre and photodiodes have been shown to be suitable for the measurements at the desired integration times. Measurements of the beam properties and the residual distributions also show that, while the detector does not currently surpass the requirements at low intensities, it is a feasible set of technologies that could be developed further to meet the specifications of the HIT clinic. An improved SNR will result from the addition of a mirror, as well as sampling the narrower beam further upstream. Dedicated electronics rather than a commercial product should significantly reduce the electronics noise. Producing ribbons with only two layers of scintillating fibre will reduce the material in the beam to acceptable levels.

Acknowledgments

We wish to thank the staff and scientists of HIT for the fruitful and productive discussions regarding the detector development and for providing us with the beam time in the experimental room. We also wish to thank the LHCb Scintillating Fibre Tracker collaboration for providing us with a sample of a scintillating fibre ribbon for our measurements.

References

[1] Th. Haberer *et al.*, *The heidelberg ion therapy center*, *Radiotherapy & Oncology*, 73 (Suppl (2)) (2004), pg. 186 [https://doi.org/10.1016/S0167-8140(04)80046-X].

[2] Th. Haberer *et al.*, *Magnetic scanning system for heavy ion therapy*, *Nucl. Instr. and Meth. A*, **330** (1993), pg. 305 [https://doi.org/10.1016/0168-9002(93)91335-K].

[3] D. Ondreka and U. Weinrich, *The Heidelberg Ion Therapy (HIT) Accelerator Coming into Operation*, *Conf. Proc. C* **0806233**, TUOCG01 (2008) [INSPIRE-CONFP,C0806233,TUOCG01].

[4] C. Schoemers *et al.*, *The intensity feedback system at Heidelberg Ion-Beam Therapy Centre*, *Nucl. Instr. and Meth. A* **795** (2015), pg. 92-99 [https://doi.org/10.1016/j.nima.2015.05.054].

[5] The LHCb Collaboration, *LHCb Tracker Upgrade TDR*, CERN/LHCC 2014-001

[6] C. Joram *et al.*, *LHCb Scintillating Fibre Tracker Engineering Design Review Report: Fibres, Mats and Modules*, CERN-LHCb-PUB-2015-008 [https://cds.cern.ch/record/2004811].

[7] E. Rubio *et al.*, *The LogicBox electronic data acquisition and control system based on FPGA* [http://ew-dev.physi.uni-heidelberg.de/rubio/LogicBox/index.php/Main_Page].

[8] E. Rojatti *et al.*, *Scintillating Fibers used as Profile Monitors for the CNAO HEBT Lines* [INSPIRE-1417432].

[9] O. Borshchev *et al. Development of a New Class of Scintillating Fibres with Very Short Decay Time and High Light Yield*, *JINST* **12** P05013 (2017) [https://doi.org/10.1088/1748-0221/12/05/P05013].

[10] J.M. Berger, J.S. Coursey, M.A. Zucker and J. Chang, *ESTAR, PSTAR, and ASTAR: Computer Programs for Calculating Stopping-Power and Range Tables for Electrons, Protons, and Helium Ions (version 2.0.0)*, National Institute of Standards and Technology, Gaithersburg, MD. (2005). [NIST PSTAR Database].

[11] International Commision on Radiation Units and Measurements, *Stopping powers and ranges for protons and alpha particles*, *Tech. Rep. 49*, ICRU (1993) [NIST ASTAR Database].

[12] H. Paul and A. Schinner, *An empirical approach to the stopping power of solids and gases for ions from 3Li to 18Ar*, *Nucl. Instr. and Meth. B* **179** (2001), pg. 299-315 [https://doi.org/10.1016/S0168-583X(01)00576-6] [http://www.exphys.uni-linz.ac.at/stopping/].

[13] J.B. Birks, *Phys. Rev.* **54** (1951) 2.

[14] R. Brun and F. Rademakers, *ROOT - An Object Oriented Data Analysis Framework*, *Proceedings AIHENP'96 Workshop*, Lausanne (1996), *Nucl. Inst. & Meth. in Phys. Res. A* **389** (1997) pg. 81-86 [http://root.cern.ch/].

[15] G. Tarlé, S.P. Ahlen, B.G. Cartwright, *Astrophys. J.* **230** (1979).

[16] M. Salamon, S.P. Ahlen, *Nucl. Instr. and Meth. A* **195** (1982) 3.

[17] R. Voltz, J. Lopes da Silva, G. Laustriat, A. Coche, *Influence of the Nature of Ionizing Particles on the Specific Luminescence of Organic Scintillators*, *J. Chem. Phys.* **45** (9) (1966) 3306.

[18] D. Broggio *et al.*, *Polyvinyltoluene scintillators for relative ion dosimetry: An investigation with Helium, Carbon and Neon beams*, *Nucl. Instr. and Meth. B* **254** (2007) pg. 3-9 [https://doi.org/10.1016/j.nimb.2006.09.009].

[19] C. Joram *et al.*, *JINST* **10** C08005 (2005) [https://doi.org/10.1088/1748-0221/10/08/C08005]